

# Electron-Impact Excitation of Zirconium I-III in support of Neutron Star Merger Diagnostics

M. McCann<sup>1\*</sup>, C. P. Ballance<sup>1</sup>, F. McNeill<sup>1</sup>, S. A. Sim<sup>1</sup>, and C. A. Ramsbottom<sup>1</sup>

<sup>1</sup>*Astrophysics Research Centre, School of Mathematics and Physics, Queen's University Belfast, BT7 1NN, Northern Ireland*

Accepted XXX. Received YYY; in original form ZZZ

## ABSTRACT

Recent observation and analysis of kilonovae (KNe) spectra as a result of neutron star mergers require accurate and complete atomic structure and collisional data for interpretation. Ideally, the atomic datasets for elements predicted to be abundant in the ejecta should be experimentally calibrated. For near-neutral ion stages of Zirconium in particular, the *A*-values and the associated excitation/de-excitation rates are required from collision calculations built upon accurate structure models. The atomic orbitals required to perform the structure calculations may be calculated using a Multi-Configuration-Dirac-Fock (MCDF) approximation implemented within the General Relativistic Atomic Structure Package (GRASP0). Optimized sets of relativistic atomic orbitals are then imported into electron-impact excitation collision calculations. A relativistic *R*-matrix formulation within the Dirac Atomic R-matrix Code (DARC) is employed to compute collision strengths, which are subsequently Maxwellian convolved to produce excitation/de-excitation rates for a wide range of electron temperatures. These atomic datasets subsequently provide the foundations for non-local thermodynamic equilibrium (NLTE) collisional-radiative models. In this work all these computations have been carried out for the first three ion stages of Zirconium (Zr I-III) with the data further interfaced with collisional-radiative and radiative transfer codes to produce synthetic spectra which can be compared with observation.

**Key words:** atomic data – scattering – plasmas – techniques: spectroscopic.

## 1 INTRODUCTION

Binary neutron star mergers (NSM) have been proposed as one possible origin of heavy elements with atomic number greater than iron. In the conditions of NSM these elements are expected to be formed through the process of rapid neutron capture (*r*-process) (Kajino et al. 2019), a process which occurs when the timescale for neutron capture is shorter than the timescale for  $\beta$  decay. In NSM the comparatively large neutron flux drives the neutron capture time down. The *r*-process produces a large amount of unstable nuclei which can subsequently decay to form elements that may account for observed abundances in the universe. There has been a significant increase in activity surrounding these topics since the detection of gravitational waves from a NSM event in 2017 and subsequent observations of the produced kilonova (KNe) AT2017gfo (Pian et al. 2017; Smartt et al. 2017).

To determine if heavy species are produced in a NSM it is important to analyse the observed spectra for lines associated with high *Z* elements. However, disentangling these lines in the observed KNe spectra is a difficult endeavour. To accomplish this we require accurate synthetic spectra to compare against the KNe spectra so that we may distinguish the features, emerging from multiple ion stages, that belong

to the elements of interest. This is further complicated as the KNe plasma rapidly enters a Non-Local Thermodynamic Equilibrium (NLTE) regime at the temperatures and densities of interest, as discussed in Pognan et al. (2023). To generate a synthetic spectra for a species in a NLTE environment, accurate and complete atomic data sets are necessary, data sets which include energy levels, transition rates and excitation/de-excitation rates for all transitions among the levels of interest. In Vieira et al. (2023) Zr is suggested as one of the elements contributing to the ejecta spectrum and in Gillanders et al. (2024) one of the proposed species of interest is Zr II. This prediction was based on 1D radiative transfer simulations using the TARDIS modelling code (Kerzendorf & Sim 2014). To aid in the continued analysis of NSM this work will introduce new atomic data for the first three ion stages Zr I, Zr II and Zr III into such radiative transfer simulations.

Recent papers by Ljung et al. (2006) and Lawler et al. (2022) have reported experimental energy levels for Zr I and Zr II and oscillator strengths for transitions among these levels for Zr II. Additional calculations by Biémont et al. (1981) determined oscillator strengths for transitions in Zr I and Zr II. These works are supplemented by data listed in the National Institute of Science and Technology Atomic Spectra Database (NIST ASD) (Kramida et al. 2024), where atomic energy level data for Zr I and Zr II from Moore (1971) are reported. Experimental energy levels and oscillator strengths

\* E-mail: michael.mccann@qub.ac.uk

for Zr III are found in the early work of [Reader & Acquista \(1997\)](#). The experimental data from these publications will be used to benchmark the atomic data computed in this work. Our primary goal is comprehensive coverage of the first three ion stages of Zr that provides a reasonable representation of the atomic structure and electron-impact excitation rates to model plasmas at KNe densities and temperatures. It should be noted that there are no collisional excitation data currently available in the literature for any of the three Zr species under consideration. Additionally it is considered that excitation and dielectronic recombination may be the most relevant processes that effect the observed spectra, therefore generating the excitation data will be useful in understanding the KNe.

The generation of the atomic data is split into two sections, first an atomic structure model is constructed and secondly this model is incorporated into a collision calculation to compute the electron-impact excitation cross sections and associated parameters. The atomic structure calculation generates energy levels, oscillator strengths and spontaneous transition probabilities, from a set of orthogonal electron orbitals. The general-purpose relativistic atomic structure program (GRASP0) ([Parpia et al. 1996](#)), which uses the Multi-Configurational Dirac Fock method, is employed in the generation of the electron orbitals. These electron orbitals are then used as the starting point in the second phase, an electron-impact excitation calculation, which generates Maxwellian averaged collision rates over a wide range of electron temperatures which can be used in LTE and NLTE plasma modelling. In this second phase the fully relativistic Dirac Atomic R-matrix Codes (DARC) ([Ballance 2024](#); [Norrington & Grant 1987](#)) are used to compute the collision cross sections, these codes are well-suited to atomic species with high  $Z$  where relativistic effects are important. The underlying theory of electron-impact excitation R-matrix calculations is discussed in greater detail within [Burke \(2011\)](#) and will not be reproduced here.

The remainder of the paper is structured as follows. In Sec. 2 the atomic structure models describing the Zr I, II and III targets are discussed. The computed energy levels and transition probabilities for transitions among these levels are compared with known experimental values and other theoretical predictions from the literature. In Sec. 3 results from the corresponding electron-impact excitation calculations are reported, and some examples of both the resulting collision strengths and Maxwellian averaged effective collision strengths for selected allowed and forbidden lines are shown. In Sec. 4 the new atomic data that have been generated are incorporated into the collisional radiative modelling code ColRadPy ([Johnson et al. 2019](#)), to produce synthetic spectra. Analysing these spectra allows us to test the accuracy of the data and probe LTE and NLTE assumptions via the level populations. In Sec. 5 the Zr data is incorporated into the 1D radiative transfer TARDIS code to produce synthetic spectra which are compared to the AT2017gfo observations. Finally in Sec. 6 this work on the atomic data for Zr I - III will be summarised and conclusions drawn.

Zr I		Zr II		Zr III		
Even	Odd	Even	Odd	Even	Odd	
4d <sup>2</sup> 5s <sup>2</sup>	4d <sup>2</sup> 5s5p	4d <sup>2</sup> 5s	4d <sup>2</sup> 5p	4d <sup>2</sup>	4d6d	4d4f
4d <sup>3</sup> 5s	4d5s <sup>2</sup> 5p	4d <sup>3</sup>	4d5s5p	4f <sup>2</sup>	6d <sup>2</sup>	4d5p
4d <sup>4</sup>	4d <sup>3</sup> 5p	4d5s <sup>2</sup>	4d <sup>2</sup> 6p	4d5s	6f <sup>2</sup>	4d5f
4d <sup>2</sup> 5p <sup>2</sup>	4d <sup>2</sup> 5s6p	4d <sup>2</sup> 6s		5s <sup>2</sup>	4d7s	4d6p
5s <sup>2</sup> 5p <sup>2</sup>		4d <sup>2</sup> 5d		5p <sup>2</sup>	7s <sup>2</sup>	4d6f
4d <sup>2</sup> 5s5d		4d5s6s		4d5d	7p <sup>2</sup>	4d7p
4d5s <sup>2</sup> 5d				5d <sup>2</sup>	4d7d	5s5p
5d <sup>4</sup>				5f <sup>2</sup>	7d <sup>2</sup>	
4d <sup>2</sup> 5s6s				4d6s	5s5d	
4d <sup>2</sup> 6s <sup>2</sup>				6s <sup>2</sup>	5s6s	
				6p <sup>2</sup>		

**Table 1.** Configurations included in the GRASP0 calculations for each ion stage of Zr, the electron configurations shown list the valence electrons only and each configuration includes a Kr core.

## 2 ATOMIC STRUCTURE

The atomic structure models for Zr I, II and III have been calculated using an extensively modified version of GRASP0 ([Parpia et al. 1996](#)). For Zr I the GRASP0 model included a total of 14 non-relativistic configurations, 10 of which were even parity and 4 were odd parity. This configuration set resulted in a total of 726 individual fine-structure energy levels. For Zr II the GRASP0 model included a total of 9 non-relativistic configurations, 6 of which were even parity and 3 were odd parity. This much smaller configuration set resulted in a total of 241 energy levels. Finally, for Zr III the GRASP0 calculation included a total of 28 non-relativistic configurations, 21 of which were even parity and 7 were odd parity. This configuration set resulted in a total of 265 fine-structure energy levels. In Table 1 all the configurations included for each ion stage model are listed, noting that only the valence electrons are listed and each configuration includes a Kr core.

A necessary test of atomic structure accuracy is to compare the absolute energy difference between the calculated level energies from GRASP0 with the experimentally measured values available in the NIST ASD ([Kramida et al. 2024](#)). In Table 2 we present the energies in Ryds for the first 10 even and first 10 odd levels of Zr I and compare with the listed values in [Lawler et al. \(2022\)](#). For the low-lying even levels the agreement is very good with the largest difference of 0.01 Ryds occurring for the 4d<sup>2</sup>5s<sup>2</sup> <sup>1</sup>D<sub>2</sub> (index 9) level. For the higher lying odd states the agreement consistently falls between  $\approx 0.02 - 0.04$  Ryds which is satisfactory for this neutral case. A similar table of energies is presented in Table 3 for Zr II where the comparison is made with the listed values in [Lawler et al. \(2022\)](#). Again good agreement is evident for all the even states listed, differences of at worst 0.013 Ryds are recorded. For this singly ionised system the odd states are much better behaved and agreement of less than 0.01 Ryds is found for all levels presented. Finally, in Table 4 the comparison is shown for Zr III where the NIST listed values are from [Reader & Acquista \(1997\)](#). The alignment for the even levels is again very satisfactory, the higher lying odd states display disparities between  $\approx 0.05 - 0.06$  Ryds. To graphically display this data we present, in Fig. 1, a plot of the full set of available NIST energy levels in Ryds against the GRASP0 energies for each ion species of Zr with the dashed line indicating the line

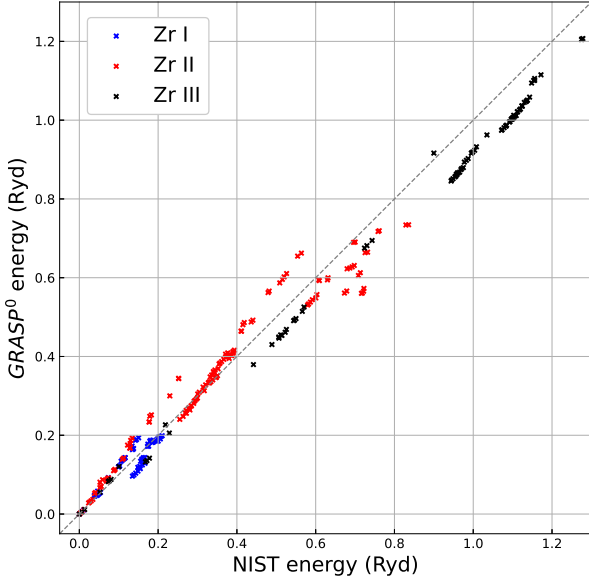


**Figure 1.** Comparison of GRASP0 energy levels for Zr I (blue), Zr II (red) and Zr III (black) with those of Lawler et al. (2022) and Reader & Acquista (1997) available in NIST ADS (Kramida et al. 2024). The dotted line represents the line of equality.

of equality. Clustering around this line for all three charge states is evident.

A further test to gauge the accuracy of the Zr I, II and III target state wavefunctions is to compare known values of the Einstein A-values for transitions among the target levels included in each model. Within GRASP0 there is an option to shift the level energies of the target to their exact experimental positions prior to the computation of the A-values. This is an important feature as the transition probabilities directly depend on the wavelength to an odd power,  $\lambda^3$  for dipole transitions (E1 and M1),  $\lambda^5$  for quadrupoles (E2 and M2) and  $\lambda^7$  for octupoles (E3 and M3). Hence, even small disparities in  $\lambda$  can lead to large inaccuracies in the computed A-values. Ensuring spectroscopically accurate values for the wavelengths should significantly improve the accuracy of the A-values and aid the identification of specific lines during the analysis of observational spectra. Note that shifting to experimental values may correct the wavelength dependence of an A-value, but not the underlying line strength. The A-values in this paper are computed using the spectroscopically accurate NIST values listed in Tables 2-4. The shifted A-value for dipole transitions can be determined by

$$A_{ij}(\text{Shifted}) = \left( \frac{\lambda_{\text{Calculated}}}{\lambda_{\text{NIST}}} \right)^3 A_{ij}(\text{Unshifted}), \quad (1)$$

where the power of 3 would be increased to 5 for quadrupoles and 7 for octupoles.

It is important to investigate the effect shifting to experimental energies, where available, has on the resulting A-values. In Fig. 2 a selection of Zr II dipole transitions (both E1 and M1) are presented for wavelengths in the region 150 – 600 nm, particularly relevant for KNe modelling. Only those transitions among the lowest 100 levels are considered. In Fig. 3

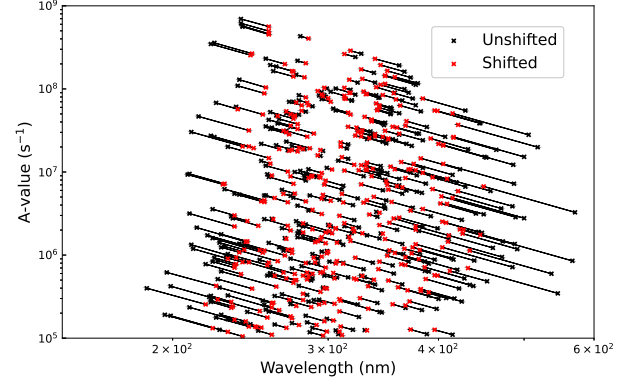


**Figure 2.** Computed A-values ( $\text{s}^{-1}$ ) for a selection of E1 and M1 dipole lines in Zr II, as a function of wavelength (nm) for computations employing a shift to NIST energy values (red) versus those where the *ab initio* energies are adopted (black).

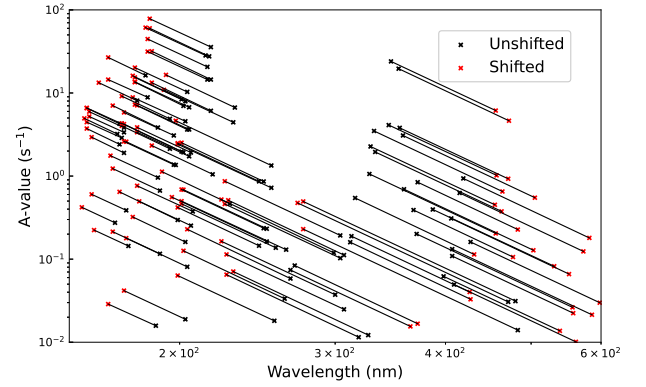


**Figure 3.** Computed A-values ( $\text{s}^{-1}$ ) for a selection of E2 and M2 quadrupole lines in Zr II, as a function of wavelength (nm) for computations employing a shift to NIST energy values (red) versus those where the *ab initio* energies are adopted (black).

a corresponding figure for a selection of quadrupole transitions in Zr II is shown. Clearly the quadrupole lines exhibit a steeper gradient between shifted and non-shifted values as expected from the different power relationship they have with wavelength, with a dependence of  $\lambda^5$  for quadrupoles rather than  $\lambda^3$  for dipoles. Additionally the magnitude of the shift gets larger at higher wavelength, because the wavelength is inversely proportional to the energy separation  $\Delta E$ , so an equivalent shift in the energy levels represents a larger proportion of the smaller  $\Delta E$  at higher wavelength. These two figures emphasise the importance of calibrating with experimental energies, where available, when computing radiative atomic data for use in spectroscopic modelling.

In Table 5 the computed A-values for the strongest E1 dipole lines of Zr I are compared to the A-values derived from oscillator strengths in Biémont et al. (1981). Only a small number of E1 lines are compared here as the target state energies available in NIST only allow for the shifting of 63 of the low lying levels. Good consistency in the order of magnitude between the experimental and calculated values is

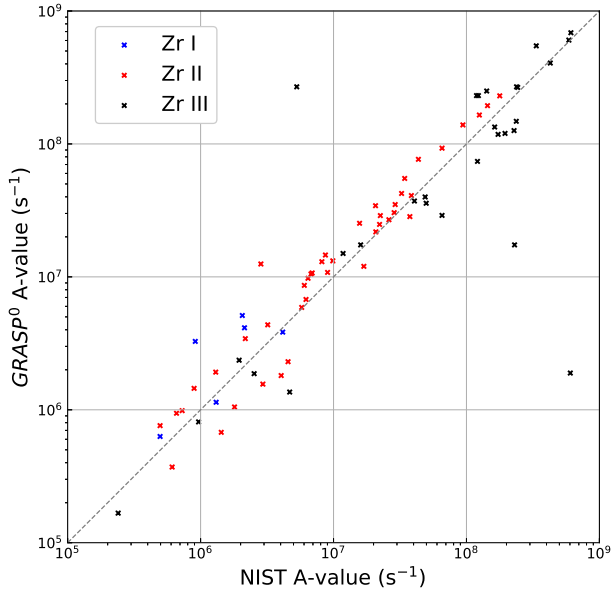


**Figure 4.** Comparison of GRASP0 A-values for Zr I (blue), Zr II (red) and Zr III (black) with those of Biémont et al. (1981); Ljung et al. (2006); Reader & Acquista (1997).

observed for all transitions considered, the largest disparity observed for the 4-48 dipole line. In Table 6 the calculated A-values for Zr II are compared with the A-values derived from oscillator strengths in Ljung et al. (2006). Again only the strong E1 lines are tabulated but there are significantly more to consider as there are many more energies available in NIST for Zr II. Again a similar broad agreement is evident between the available literature and the newly calculated A-values. Finally, in Table 7 a similar comparison for Zr III is presented. In this case, the comparison is with the A-values listed in Reader & Acquista (1997). Again good agreement is found for the majority of lines. Similar to Fig. 1 the A-values can be compared graphically, as shown in Fig. 4. As in Fig. 1 clustering around the line is evident for all the charge states.

Level	Conf.	Parity	Term	$J$	Lawler et al. (2022) (Ryd)	GRASP <sup>0</sup> (Ryd)	diff (Ryd)
1	4d <sup>2</sup> 5s <sup>2</sup>	even	<sup>3</sup> F	2	0.0000000	0.0000000	0.0000000
2	4d <sup>2</sup> 5s <sup>2</sup>	even	<sup>3</sup> F	3	0.0051980	0.0047690	-0.0004290
3	4d <sup>2</sup> 5s <sup>2</sup>	even	<sup>3</sup> F	4	0.0113074	0.0106163	-0.0006911
4	4d <sup>2</sup> 5s <sup>2</sup>	even	<sup>3</sup> P	2	0.0381466	0.0471997	0.0090531
5	4d <sup>2</sup> 5s <sup>2</sup>	even	<sup>3</sup> P	0	0.0382445	0.0448361	0.0065916
6	4d <sup>2</sup> 5s <sup>2</sup>	even	<sup>3</sup> P	1	0.0398796	0.0462170	0.0063374
7	4d <sup>3</sup> 5s <sup>1</sup>	even	<sup>5</sup> F	1	0.0443835	0.0471652	0.0027817
8	4d <sup>3</sup> 5s <sup>1</sup>	even	<sup>5</sup> F	2	0.0457767	0.0482713	0.0024946
9	4d <sup>2</sup> 5s <sup>2</sup>	even	<sup>1</sup> D	2	0.0464899	0.0580415	0.0115516
10	4d <sup>3</sup> 5s <sup>1</sup>	even	<sup>5</sup> F	3	0.0478330	0.0499145	0.0020815
26	4d <sup>2</sup> 5s <sup>1</sup> 5p <sup>1</sup>	odd	<sup>5</sup> G	2	0.1347175	0.0961847	-0.0385328
30	4d <sup>2</sup> 5s <sup>1</sup> 5p <sup>1</sup>	odd	<sup>5</sup> G	3	0.1385241	0.0994675	-0.0390566
33	4d <sup>2</sup> 5s <sup>1</sup> 5p <sup>1</sup>	odd	<sup>5</sup> G	4	0.1432545	0.1037616	-0.0394928
37	4d <sup>2</sup> 5s <sup>1</sup> 5p <sup>1</sup>	odd	<sup>5</sup> F	2	0.1485047	0.1186320	-0.0298726
38	4d <sup>2</sup> 5s <sup>1</sup> 5p <sup>1</sup>	odd	<sup>5</sup> G	5	0.1486911	0.1089937	-0.0396974
41	4d <sup>2</sup> 5s <sup>1</sup> 5p <sup>1</sup>	odd	<sup>5</sup> F	1	0.1529738	0.1168793	-0.0360945
42	4d <sup>2</sup> 5s <sup>1</sup> 5p <sup>1</sup>	odd	<sup>5</sup> F	3	0.1534932	0.1212376	-0.0322556
44	4d <sup>2</sup> 5s <sup>1</sup> 5p <sup>1</sup>	odd	<sup>5</sup> G	6	0.1547176	0.1150933	-0.0396243
45	4d <sup>2</sup> 5s <sup>1</sup> 5p <sup>1</sup>	odd	<sup>3</sup> F	2	0.1554586	0.1340496	-0.0214090
46	4d <sup>2</sup> 5s <sup>1</sup> 5p <sup>1</sup>	odd	<sup>3</sup> F	3	0.1587625	0.1374634	-0.0212991

Table 2: Comparison between the first 10 even and the first 10 odd energy levels from the GRASP<sup>0</sup> calculation of Zr I with energies from Lawler et al. (2022), in Ryds. The index numbers of the levels are from the energy order of the shifted calculation.

Level	Conf.	Parity	Term	$J$	Lawler et al. (2022) (Ryd)	GRASP <sup>0</sup> (Ryd)	diff (Ryd)
1	4d <sup>2</sup> 5s <sup>1</sup>	even	<sup>4</sup> F	1.5	0.0000000	0.0000000	0.0000000
2	4d <sup>2</sup> 5s <sup>1</sup>	even	<sup>4</sup> F	2.5	0.0028675	0.0027692	-0.0000983
3	4d <sup>2</sup> 5s <sup>1</sup>	even	<sup>4</sup> F	3.5	0.0069570	0.0066571	-0.0002999
4	4d <sup>2</sup> 5s <sup>1</sup>	even	<sup>4</sup> F	4.5	0.0120552	0.0115605	-0.0004947
5	4d <sup>3</sup>	even	<sup>4</sup> F	1.5	0.0234397	0.0281406	0.0047009
6	4d <sup>3</sup>	even	<sup>4</sup> F	2.5	0.0263816	0.0304560	0.0040744
7	4d <sup>3</sup>	even	<sup>4</sup> F	3.5	0.0300685	0.0335215	0.0034530
8	4d <sup>3</sup>	even	<sup>4</sup> F	4.5	0.0342423	0.0372035	0.0029612
9	4d <sup>2</sup> 5s <sup>1</sup>	even	<sup>2</sup> D	1.5	0.0387134	0.0522989	0.0135855
10	4d <sup>2</sup> 5s <sup>1</sup>	even	<sup>2</sup> D	2.5	0.0410571	0.0548323	0.0137752
38	4d <sup>2</sup> 5p <sup>1</sup>	odd	<sup>4</sup> G	2.5	0.2550074	0.2403789	-0.0146285
39	4d <sup>2</sup> 5p <sup>1</sup>	odd	<sup>4</sup> G	3.5	0.2634386	0.2478361	-0.0156025
40	4d <sup>2</sup> 5p <sup>1</sup>	odd	<sup>2</sup> F	2.5	0.2688691	0.2569563	-0.0119128
41	4d <sup>2</sup> 5p <sup>1</sup>	odd	<sup>2</sup> D	1.5	0.2713535	0.2630735	-0.0082799
42	4d <sup>2</sup> 5p <sup>1</sup>	odd	<sup>4</sup> G	4.5	0.2719209	0.2557986	-0.0161222
43	4d <sup>2</sup> 5p <sup>1</sup>	odd	<sup>4</sup> F	1.5	0.2773476	0.2679613	-0.0093863
44	4d <sup>2</sup> 5p <sup>1</sup>	odd	<sup>4</sup> F	2.5	0.2784056	0.2692824	-0.0091231
45	4d <sup>2</sup> 5p <sup>1</sup>	odd	<sup>2</sup> F	3.5	0.2784992	0.2673287	-0.0111705
46	4d <sup>2</sup> 5p <sup>1</sup>	odd	<sup>4</sup> G	5.5	0.2806314	0.2643171	-0.0163142
47	4d <sup>2</sup> 5p <sup>1</sup>	odd	<sup>2</sup> D	2.5	0.2839512	0.2744373	-0.0095139

Table 3: Comparison between the first 10 even and the first 10 odd energy levels from the GRASP<sup>0</sup> calculation of Zr II with energies from Lawler et al. (2022), in Ryds. The index numbers of the levels are from the energy order of the shifted calculation.

Level	Conf.	Parity	Term	$J$	Reader & Acquista (1997) (Ryd)	GRASP <sup>0</sup> (Ryd)	diff (Ryd)
1	4d <sup>2</sup>	even	<sup>3</sup> F	2	0.0000000	0.0000000	0.0000000
2	4d <sup>2</sup>	even	<sup>3</sup> F	3	0.0062111	0.0051968	-0.0010143
3	4d <sup>2</sup>	even	<sup>3</sup> F	4	0.0135455	0.0115437	-0.0020018
4	4d <sup>2</sup>	even	<sup>1</sup> D	2	0.0523376	0.0552481	0.0029105
5	4d <sup>2</sup>	even	<sup>3</sup> P	0	0.0734812	0.0824057	0.0089245
6	4d <sup>2</sup>	even	<sup>3</sup> P	1	0.0758823	0.0843364	0.0084541
7	4d <sup>2</sup>	even	<sup>3</sup> P	2	0.0805557	0.0880235	0.0074678
8	4d <sup>2</sup>	even	<sup>1</sup> G	4	0.1007002	0.1207737	0.0200735
9	4d <sup>1</sup> 5s <sup>1</sup>	even	<sup>3</sup> D	1	0.1676838	0.1323546	-0.0353292
10	4d <sup>1</sup> 5s <sup>1</sup>	even	<sup>3</sup> D	2	0.1713665	0.1358710	-0.0354955
15	4d <sup>1</sup> 5p <sup>1</sup>	odd	<sup>1</sup> D	2	0.4888847	0.4302977	-0.0585871
16	4d <sup>1</sup> 5p <sup>1</sup>	odd	<sup>3</sup> F	2	0.5062779	0.4494225	-0.0568555
17	4d <sup>1</sup> 5p <sup>1</sup>	odd	<sup>3</sup> D	1	0.5068091	0.4465398	-0.0602693
18	4d <sup>1</sup> 5p <sup>1</sup>	odd	<sup>3</sup> F	3	0.5110139	0.4548248	-0.0561891
19	4d <sup>1</sup> 5p <sup>1</sup>	odd	<sup>3</sup> D	2	0.5142987	0.4534983	-0.0608005
20	4d <sup>1</sup> 5p <sup>1</sup>	odd	<sup>3</sup> D	3	0.5226011	0.4614351	-0.0611661
21	4d <sup>1</sup> 5p <sup>1</sup>	odd	<sup>3</sup> F	4	0.5256563	0.4687638	-0.0568925
22	4d <sup>1</sup> 5p <sup>1</sup>	odd	<sup>3</sup> P	1	0.5440215	0.4908779	-0.0531436
23	4d <sup>1</sup> 5p <sup>1</sup>	odd	<sup>3</sup> P	0	0.5462827	0.4924677	-0.0538151
24	4d <sup>1</sup> 5p <sup>1</sup>	odd	<sup>3</sup> P	2	0.5500259	0.4962671	-0.0537589

Table 4: Comparison between the first 10 even and the first 10 odd energy levels from the GRASP<sup>0</sup> calculation of Zr III with energies from Reader & Acquista (1997), in Ryds. The index numbers of the levels are from the energy order of the shifted calculation.

Level	Lower				Level	upper				A-values (s <sup>-1</sup> )	
	Conf.	Parity	Term	$J$		Conf.	Parity	Term	$J$	GRASP <sup>0</sup>	Biémont et al. (1981)
1	4d <sup>2</sup> 5s <sup>2</sup>	even	<sup>3</sup> F	2	45	4d <sup>2</sup> 5s <sup>1</sup> 5p <sup>1</sup>	odd	<sup>3</sup> F	2	5.12E+06	2.06E+06
2	4d <sup>2</sup> 5s <sup>2</sup>	even	<sup>3</sup> F	3	46	4d <sup>2</sup> 5s <sup>1</sup> 5p <sup>1</sup>	odd	<sup>3</sup> F	3	4.14E+06	2.14E+06
4	4d <sup>2</sup> 5s <sup>2</sup>	even	<sup>3</sup> P	2	48	4d <sup>2</sup> 5s <sup>1</sup> 5p <sup>1</sup>	odd	<sup>3</sup> P	2	3.27E+06	9.12E+05
8	4d <sup>3</sup> 5s <sup>1</sup>	even	<sup>5</sup> F	2	50	4d <sup>2</sup> 5s <sup>1</sup> 5p <sup>1</sup>	odd	<sup>5</sup> D	2	1.14E+06	1.31E+06
11	4d <sup>3</sup> 5s <sup>1</sup>	even	<sup>5</sup> F	4	52	4d <sup>2</sup> 5s <sup>1</sup> 5p <sup>1</sup>	odd	<sup>5</sup> D	3	3.84E+06	4.15E+06
11	4d <sup>3</sup> 5s <sup>1</sup>	even	<sup>5</sup> F	4	53	4d <sup>2</sup> 5s <sup>1</sup> 5p <sup>1</sup>	odd	<sup>5</sup> F	5	6.30E+05	4.96E+05

Table 5: Comparison between the A-values from the GRASP<sup>0</sup> calculation of Zr I, with A-values from Biémont et al. (1981). The index numbers of the levels are from the energy order of the shifted calculation.

Level	Lower				Level	upper				A-values ( $s^{-1}$ )	
	Conf.	Parity	Term	J		Conf.	Parity	Term	J	GRASP <sup>0</sup>	Ljung et al. (2006)
1	4d <sup>2</sup> 5s <sup>1</sup>	even	<sup>4</sup> F	1.5	38	4d <sup>2</sup> 5p <sup>1</sup>	odd	<sup>4</sup> G	2.5	1.39E+08	9.40E+07
1	4d <sup>2</sup> 5s <sup>1</sup>	even	<sup>4</sup> F	1.5	40	4d <sup>2</sup> 5p <sup>1</sup>	odd	<sup>2</sup> F	2.5	2.84E+07	3.75E+07
1	4d <sup>2</sup> 5s <sup>1</sup>	even	<sup>4</sup> F	1.5	41	4d <sup>2</sup> 5p <sup>1</sup>	odd	<sup>2</sup> D	1.5	4.24E+07	3.25E+07
1	4d <sup>2</sup> 5s <sup>1</sup>	even	<sup>4</sup> F	1.5	43	4d <sup>2</sup> 5p <sup>1</sup>	odd	<sup>4</sup> F	1.5	9.29E+07	6.55E+07
1	4d <sup>2</sup> 5s <sup>1</sup>	even	<sup>4</sup> F	1.5	47	4d <sup>2</sup> 5p <sup>1</sup>	odd	<sup>2</sup> D	2.5	1.92E+06	1.30E+06
2	4d <sup>2</sup> 5s <sup>1</sup>	even	<sup>4</sup> F	2.5	38	4d <sup>2</sup> 5p <sup>1</sup>	odd	<sup>4</sup> G	2.5	2.89E+07	2.25E+07
2	4d <sup>2</sup> 5s <sup>1</sup>	even	<sup>4</sup> F	2.5	39	4d <sup>2</sup> 5p <sup>1</sup>	odd	<sup>4</sup> G	3.5	1.65E+08	1.25E+08
2	4d <sup>2</sup> 5s <sup>1</sup>	even	<sup>4</sup> F	2.5	40	4d <sup>2</sup> 5p <sup>1</sup>	odd	<sup>2</sup> F	2.5	2.30E+06	4.55E+06
2	4d <sup>2</sup> 5s <sup>1</sup>	even	<sup>4</sup> F	2.5	41	4d <sup>2</sup> 5p <sup>1</sup>	odd	<sup>2</sup> D	1.5	2.69E+07	2.61E+07
2	4d <sup>2</sup> 5s <sup>1</sup>	even	<sup>4</sup> F	2.5	43	4d <sup>2</sup> 5p <sup>1</sup>	odd	<sup>4</sup> F	1.5	1.30E+07	8.17E+06
2	4d <sup>2</sup> 5s <sup>1</sup>	even	<sup>4</sup> F	2.5	45	4d <sup>2</sup> 5p <sup>1</sup>	odd	<sup>2</sup> F	3.5	1.20E+07	1.69E+07
2	4d <sup>2</sup> 5s <sup>1</sup>	even	<sup>4</sup> F	2.5	47	4d <sup>2</sup> 5p <sup>1</sup>	odd	<sup>2</sup> D	2.5	3.04E+07	2.86E+07
3	4d <sup>2</sup> 5s <sup>1</sup>	even	<sup>4</sup> F	3.5	38	4d <sup>2</sup> 5p <sup>1</sup>	odd	<sup>4</sup> G	2.5	9.42E+05	6.59E+05
3	4d <sup>2</sup> 5s <sup>1</sup>	even	<sup>4</sup> F	3.5	39	4d <sup>2</sup> 5p <sup>1</sup>	odd	<sup>4</sup> G	3.5	3.50E+07	2.91E+07
3	4d <sup>2</sup> 5s <sup>1</sup>	even	<sup>4</sup> F	3.5	40	4d <sup>2</sup> 5p <sup>1</sup>	odd	<sup>2</sup> F	2.5	1.56E+06	2.94E+06
3	4d <sup>2</sup> 5s <sup>1</sup>	even	<sup>4</sup> F	3.5	42	4d <sup>2</sup> 5p <sup>1</sup>	odd	<sup>4</sup> G	4.5	1.94E+08	1.44E+08
4	4d <sup>2</sup> 5s <sup>1</sup>	even	<sup>4</sup> F	4.5	42	4d <sup>2</sup> 5p <sup>1</sup>	odd	<sup>4</sup> G	4.5	2.48E+07	2.22E+07
4	4d <sup>2</sup> 5s <sup>1</sup>	even	<sup>4</sup> F	4.5	45	4d <sup>2</sup> 5p <sup>1</sup>	odd	<sup>2</sup> F	3.5	6.77E+05	1.43E+06
4	4d <sup>2</sup> 5s <sup>1</sup>	even	<sup>4</sup> F	4.5	46	4d <sup>2</sup> 5p <sup>1</sup>	odd	<sup>4</sup> G	5.5	2.30E+08	1.78E+08
5	4d <sup>3</sup>	even	<sup>4</sup> F	1.5	38	4d <sup>2</sup> 5p <sup>1</sup>	odd	<sup>4</sup> G	2.5	8.63E+06	6.03E+06
5	4d <sup>3</sup>	even	<sup>4</sup> F	1.5	41	4d <sup>2</sup> 5p <sup>1</sup>	odd	<sup>2</sup> D	1.5	4.09E+07	3.85E+07
5	4d <sup>3</sup>	even	<sup>4</sup> F	1.5	43	4d <sup>2</sup> 5p <sup>1</sup>	odd	<sup>4</sup> F	1.5	3.43E+07	2.07E+07
5	4d <sup>3</sup>	even	<sup>4</sup> F	1.5	47	4d <sup>2</sup> 5p <sup>1</sup>	odd	<sup>2</sup> D	2.5	9.85E+05	7.27E+05
6	4d <sup>3</sup>	even	<sup>4</sup> F	2.5	39	4d <sup>2</sup> 5p <sup>1</sup>	odd	<sup>4</sup> G	3.5	9.76E+06	6.43E+06
6	4d <sup>3</sup>	even	<sup>4</sup> F	2.5	41	4d <sup>2</sup> 5p <sup>1</sup>	odd	<sup>2</sup> D	1.5	3.43E+06	2.17E+06
6	4d <sup>3</sup>	even	<sup>4</sup> F	2.5	43	4d <sup>2</sup> 5p <sup>1</sup>	odd	<sup>4</sup> F	1.5	1.32E+07	9.87E+06
6	4d <sup>3</sup>	even	<sup>4</sup> F	2.5	47	4d <sup>2</sup> 5p <sup>1</sup>	odd	<sup>2</sup> D	2.5	4.36E+06	3.20E+06
7	4d <sup>3</sup>	even	<sup>4</sup> F	3.5	40	4d <sup>2</sup> 5p <sup>1</sup>	odd	<sup>2</sup> F	2.5	3.71E+05	6.11E+05
7	4d <sup>3</sup>	even	<sup>4</sup> F	3.5	42	4d <sup>2</sup> 5p <sup>1</sup>	odd	<sup>4</sup> G	4.5	1.05E+07	6.77E+06
7	4d <sup>3</sup>	even	<sup>4</sup> F	3.5	45	4d <sup>2</sup> 5p <sup>1</sup>	odd	<sup>2</sup> F	3.5	7.60E+05	4.96E+05
7	4d <sup>3</sup>	even	<sup>4</sup> F	3.5	47	4d <sup>2</sup> 5p <sup>1</sup>	odd	<sup>2</sup> D	2.5	6.76E+06	6.21E+06
8	4d <sup>3</sup>	even	<sup>4</sup> F	4.5	45	4d <sup>2</sup> 5p <sup>1</sup>	odd	<sup>2</sup> F	3.5	1.05E+06	1.80E+06
8	4d <sup>3</sup>	even	<sup>4</sup> F	4.5	46	4d <sup>2</sup> 5p <sup>1</sup>	odd	<sup>4</sup> G	5.5	1.07E+07	6.91E+06
9	4d <sup>2</sup> 5s <sup>1</sup>	even	<sup>2</sup> D	1.5	38	4d <sup>2</sup> 5p <sup>1</sup>	odd	<sup>4</sup> G	2.5	5.89E+06	5.76E+06
9	4d <sup>2</sup> 5s <sup>1</sup>	even	<sup>2</sup> D	1.5	40	4d <sup>2</sup> 5p <sup>1</sup>	odd	<sup>2</sup> F	2.5	5.50E+07	3.43E+07
9	4d <sup>2</sup> 5s <sup>1</sup>	even	<sup>2</sup> D	1.5	41	4d <sup>2</sup> 5p <sup>1</sup>	odd	<sup>2</sup> D	1.5	2.53E+07	1.57E+07
9	4d <sup>2</sup> 5s <sup>1</sup>	even	<sup>2</sup> D	1.5	43	4d <sup>2</sup> 5p <sup>1</sup>	odd	<sup>4</sup> F	1.5	1.46E+07	8.69E+06
9	4d <sup>2</sup> 5s <sup>1</sup>	even	<sup>2</sup> D	1.5	47	4d <sup>2</sup> 5p <sup>1</sup>	odd	<sup>2</sup> D	2.5	1.08E+07	9.02E+06
10	4d <sup>2</sup> 5s <sup>1</sup>	even	<sup>2</sup> D	2.5	38	4d <sup>2</sup> 5p <sup>1</sup>	odd	<sup>4</sup> G	2.5	1.81E+06	4.04E+06
10	4d <sup>2</sup> 5s <sup>1</sup>	even	<sup>2</sup> D	2.5	39	4d <sup>2</sup> 5p <sup>1</sup>	odd	<sup>4</sup> G	3.5	1.45E+06	8.94E+05
10	4d <sup>2</sup> 5s <sup>1</sup>	even	<sup>2</sup> D	2.5	40	4d <sup>2</sup> 5p <sup>1</sup>	odd	<sup>2</sup> F	2.5	2.18E+07	2.08E+07
10	4d <sup>2</sup> 5s <sup>1</sup>	even	<sup>2</sup> D	2.5	45	4d <sup>2</sup> 5p <sup>1</sup>	odd	<sup>2</sup> F	3.5	7.66E+07	4.35E+07
10	4d <sup>2</sup> 5s <sup>1</sup>	even	<sup>2</sup> D	2.5	47	4d <sup>2</sup> 5p <sup>1</sup>	odd	<sup>2</sup> D	2.5	1.25E+07	2.84E+06

Table 6: Comparison between the A-values from the GRASP<sup>0</sup> calculation of Zr II, with A-values from Ljung et al. (2006). The index numbers of the levels are from the energy order of the shifted calculation.

Level	Lower				upper					A-values ( $s^{-1}$ )	
	Conf.	Parity	Term	J	Level	Conf.	Parity	Term	J	GRASP <sup>0</sup>	Reader & Acquista (1997)
1	4d <sup>2</sup>	even	<sup>3</sup> F	2	15	4d <sup>1</sup> 5p <sup>1</sup>	odd	<sup>1</sup> D	2	7.39E+07	1.21E+08
1	4d <sup>2</sup>	even	<sup>3</sup> F	2	16	4d <sup>1</sup> 5p <sup>1</sup>	odd	<sup>3</sup> F	2	2.31E+08	1.23E+08
1	4d <sup>2</sup>	even	<sup>3</sup> F	2	17	4d <sup>1</sup> 5p <sup>1</sup>	odd	<sup>3</sup> D	1	6.86E+08	6.10E+08
2	4d <sup>2</sup>	even	<sup>3</sup> F	3	18	4d <sup>1</sup> 5p <sup>1</sup>	odd	<sup>3</sup> F	3	2.69E+08	2.38E+08
2	4d <sup>2</sup>	even	<sup>3</sup> F	3	19	4d <sup>1</sup> 5p <sup>1</sup>	odd	<sup>3</sup> D	2	6.04E+08	5.89E+08
2	4d <sup>2</sup>	even	<sup>3</sup> F	3	21	4d <sup>1</sup> 5p <sup>1</sup>	odd	<sup>3</sup> F	4	1.74E+07	1.60E+07
3	4d <sup>2</sup>	even	<sup>3</sup> F	4	18	4d <sup>1</sup> 5p <sup>1</sup>	odd	<sup>3</sup> F	3	2.69E+08	5.29E+06
3	4d <sup>2</sup>	even	<sup>3</sup> F	4	20	4d <sup>1</sup> 5p <sup>1</sup>	odd	<sup>3</sup> D	3	1.89E+06	6.04E+08
3	4d <sup>2</sup>	even	<sup>3</sup> F	4	21	4d <sup>1</sup> 5p <sup>1</sup>	odd	<sup>3</sup> F	4	1.74E+07	2.30E+08
4	4d <sup>2</sup>	even	<sup>1</sup> D	2	15	4d <sup>1</sup> 5p <sup>1</sup>	odd	<sup>1</sup> D	2	5.47E+08	3.35E+08
4	4d <sup>2</sup>	even	<sup>1</sup> D	2	16	4d <sup>1</sup> 5p <sup>1</sup>	odd	<sup>3</sup> F	2	1.26E+08	2.28E+08
5	4d <sup>2</sup>	even	<sup>3</sup> P	0	17	4d <sup>1</sup> 5p <sup>1</sup>	odd	<sup>3</sup> D	1	3.72E+07	4.06E+07
6	4d <sup>2</sup>	even	<sup>3</sup> P	1	17	4d <sup>1</sup> 5p <sup>1</sup>	odd	<sup>3</sup> D	1	1.50E+07	1.18E+07
6	4d <sup>2</sup>	even	<sup>3</sup> P	1	19	4d <sup>1</sup> 5p <sup>1</sup>	odd	<sup>3</sup> D	2	3.58E+07	4.98E+07
7	4d <sup>2</sup>	even	<sup>3</sup> P	2	15	4d <sup>1</sup> 5p <sup>1</sup>	odd	<sup>1</sup> D	2	1.87E+06	2.53E+06
7	4d <sup>2</sup>	even	<sup>3</sup> P	2	16	4d <sup>1</sup> 5p <sup>1</sup>	odd	<sup>3</sup> F	2	2.36E+06	1.95E+06
7	4d <sup>2</sup>	even	<sup>3</sup> P	2	20	4d <sup>1</sup> 5p <sup>1</sup>	odd	<sup>3</sup> D	3	3.99E+07	4.89E+07
8	4d <sup>2</sup>	even	<sup>1</sup> G	4	18	4d <sup>1</sup> 5p <sup>1</sup>	odd	<sup>3</sup> F	3	8.11E+05	9.66E+05
8	4d <sup>2</sup>	even	<sup>1</sup> G	4	20	4d <sup>1</sup> 5p <sup>1</sup>	odd	<sup>3</sup> D	3	1.36E+06	4.68E+06
8	4d <sup>2</sup>	even	<sup>1</sup> G	4	21	4d <sup>1</sup> 5p <sup>1</sup>	odd	<sup>3</sup> F	4	1.67E+05	2.40E+05
9	4d <sup>1</sup> 5s <sup>1</sup>	even	<sup>3</sup> D	1	15	4d <sup>1</sup> 5p <sup>1</sup>	odd	<sup>1</sup> D	2	2.90E+07	6.55E+07
9	4d <sup>1</sup> 5s <sup>1</sup>	even	<sup>3</sup> D	1	16	4d <sup>1</sup> 5p <sup>1</sup>	odd	<sup>3</sup> F	2	1.18E+08	1.73E+08
9	4d <sup>1</sup> 5s <sup>1</sup>	even	<sup>3</sup> D	1	17	4d <sup>1</sup> 5p <sup>1</sup>	odd	<sup>3</sup> D	1	2.66E+08	2.43E+08
9	4d <sup>1</sup> 5s <sup>1</sup>	even	<sup>3</sup> D	1	19	4d <sup>1</sup> 5p <sup>1</sup>	odd	<sup>3</sup> D	2	2.31E+08	1.19E+08
9	4d <sup>1</sup> 5s <sup>1</sup>	even	<sup>3</sup> D	1	22	4d <sup>1</sup> 5p <sup>1</sup>	odd	<sup>3</sup> P	1	1.34E+08	1.63E+08
9	4d <sup>1</sup> 5s <sup>1</sup>	even	<sup>3</sup> D	1	23	4d <sup>1</sup> 5p <sup>1</sup>	odd	<sup>3</sup> P	0	4.06E+08	4.27E+08
10	4d <sup>1</sup> 5s <sup>1</sup>	even	<sup>3</sup> D	2	18	4d <sup>1</sup> 5p <sup>1</sup>	odd	<sup>3</sup> F	3	1.48E+08	2.37E+08
10	4d <sup>1</sup> 5s <sup>1</sup>	even	<sup>3</sup> D	2	19	4d <sup>1</sup> 5p <sup>1</sup>	odd	<sup>3</sup> D	2	1.20E+08	1.95E+08
10	4d <sup>1</sup> 5s <sup>1</sup>	even	<sup>3</sup> D	2	20	4d <sup>1</sup> 5p <sup>1</sup>	odd	<sup>3</sup> D	3	2.50E+08	1.42E+08

Table 7: Comparison between the A-values from the GRASP<sup>0</sup> calculation of Zr III, with A-values from Reader & Acquista (1997). The index numbers of the levels are from the energy order of the shifted calculation.



### 3 ELECTRON-IMPACT EXCITATION

Using the parallel version of the Dirac Atomic R-matrix code DARC (Ballance 2024; Norrington & Grant 1987) electron-impact excitation calculations for Zr I - III were performed using the structure models outlined in Sec. 2. A discussion of each of these three collision calculations is given below.

For Zr I, 150 levels were maintained in the close-coupling expansion out of a possible 726 levels included in the CI description of the target. This number was chosen to keep the computations to a manageable size, to ensure that the energies of the target states could be shifted to their experimentally known positions and also to ensure that the relevant KNe temperature range was spanned. The calculations included 78 partial waves with a total angular momentum of  $2J = 1 - 77$  with a maximum of 924 channels and a maximum Hamiltonian matrix size of 28028. A continuum basis size of 30 was adopted in the computations. The grid of incident electron energies over which the collision strengths were computed for the low partial waves ( $2J = 1 - 29$ ) ranged from 0.0 - 4.0 Ryds, where 0.0 - 0.6 Ryds was a fine mesh spacing of 0.00002 Ryds representing 30,000 individual energy points and 0.6 - 4.0 Ryds used a coarser mesh with a spacing of 0.0034 Ryds including 1000 energy points. For the higher partial waves ( $2J = 31 - 77$ ) where the resonance contributions are considerably less, a coarse mesh of 0.01 Ryds ranging from 0.0 - 4.0 Ryds. A top-up procedure (Burgess 1974) was applied to account for contributions from partial waves  $2J \geq 77$ , important to ensure that all contributions to the slowing converging allowed lines were included. Infinite energy points for the dipoles were also computed for completeness. It is implicit that the calculation of infinite energy points and the top-up procedure is employed for the remaining two ion stages.

The comparable calculations for Zr II included all of the possible 241 target levels from the set of target configurations. In the electron-impact scattering model, 78 partial waves with total angular momentum  $2J = 0 - 76$  were included, with a continuum basis size of 20, a maximum of 1460 channels, resulting in a maximum Hamiltonian matrix size of 29230. A fine mesh of energies with spacing 0.00003125 Ryds was used for the low partial waves between 0.0 - 1.0 Ryds and a coarser mesh of 0.003 Ryds between 1.0 - 4.0 Ryds, with a coarse mesh of 0.004 Ryds between 0.0 - 4.0 Ryds for the higher partial waves.

Finally, for Zr III 167 out of the possible 265 target levels were included, with 78 partial waves with  $2J = 1 - 77$ , a continuum basis size of 30, a maximum of 917 channels, and a maximum matrix size of 43701. A fine mesh of 0.00004 Ryds and a coarse grid with spacing 0.002 Ryds were adopted for the low partial waves between 0.0 - 2.0 Ryds and 2.0 - 4.0 Ryds respectively, with a coarse mesh of 0.01 Ryds between 0.0 - 4.0 Ryds for the higher partial waves.

Three of the lowest-lying, strongest dipole transitions from the ground state for each species have been selected as representative examples from the collision calculations. For Zr I the transitions 1-26, 1-30 and 1-41 were chosen, these indexes are from Table 2 and are for transitions among levels 1:  $4d^25s^2\ ^3F_2$ , 26:  $4d^25s5p\ ^5G_2$ , 30:  $4d^25s5p\ ^5G_3$  and 41:  $4d^25s5p\ ^5F_1$ . The collision strengths as a function of incident electron energy in Ryds for these three transitions are shown in Fig. 5a and the corresponding Maxwellian averaged effective colli-

sion strengths are shown in Fig. 5b as a function of electron temperature in Kelvin. Clearly evident are the Rydberg resonances converging onto the target state thresholds in the low-energy region, followed by the smooth background cross section at higher energies. For these spin-changing M1 lines the collision strengths remain relatively constant for energies above approximately 2 Ryds. The corresponding effective collision strengths, depicted in Fig. 5b replicate this behaviour, the resonance features causing an enhancement at low temperatures with the effective rates reaching a near constant value for the higher temperatures considered.

For Zr II the transitions chosen were 1-38, 1-40 and 1-41, these indexes are from Table 3 and are for transitions among levels 1:  $4d^25s\ ^4F_{3/2}$ , 38:  $4d^25p\ ^4G_{5/2}$ , 40:  $4d^25p\ ^2F_{5/2}$  and 41:  $4d^25p\ ^4F_{3/2}$ . Transition 1-38 represents a strong E1 dipole and the collision strength for this transition, shown in Fig. 5c (black) exhibits the correct behaviour of a steep rise towards the high energy limit as the incident electron energy increases. The corresponding effective collision strength shown in Fig. 5d mirrors this trend. Transitions 1-40 and 1-41 represent spin-changing M1 dipoles for which the collision strengths show a less pronounced rise of the background cross section at higher energies, as expected. Finally, for Zr III the collision strengths for transitions 1-15, 1-16 and 1-17 are plotted in Fig. 5e, and the corresponding effective collision strengths in Fig. 5f. These indexes are from Table 4 and are for transitions between levels 1:  $4d^2\ ^3F_2$ , 15:  $4d5p\ ^1D_2$ , 16:  $4d5p\ ^3F_2$  and 17:  $4d5p\ ^3D_1$ .

In Sec. 2 the effect on the A-values due to calibrating the energy levels to their measured experimental positions was carefully analysed. For consistency a similar investigation is carried out here to examine the effect, if any, on the collision strengths and effective collision strengths due to implementing an energy shift on the target level positions during the electron-impact excitation computations. The impact of this is shown in Fig. 6 for the same three example transitions for Zr II plotted in Fig. 5. Transition 1-38 ( $4d^25s\ ^4F_{3/2}$ - $4d^25p\ ^4G_{5/2}$ ) is shown in Fig. 6a, transition 1-40 ( $4d^25s\ ^4F_{3/2}$ - $4d^25p\ ^2F_{5/2}$ ) in Fig. 6b and finally transition 1-41 ( $4d^25s\ ^4F_{3/2}$ - $4d^25p\ ^4F_{3/2}$ ) in Fig. 6c. From these comparisons we can conclude that the effect of fine-tuning the diagonal elements of the energy Hamiltonian during the collision calculation has little effect on the final collision strengths at all incident electron energies, and hence will not significantly alter the corresponding effective collision strengths. A considerable effort was made to scrutinise a large selection of dipole and quadrupole transitions for all three charge states of Zr to ensure that this statement was corroborated.

### 4 COLLISIONAL MODELLING

Using the Python COLRADPY codes (Johnson et al. 2019), based on the collisional radiative theory of Summers et al. (2006), synthetic spectra can be generated for Zr using this newly calculated atomic data. In this section we concentrate on the computation of the excitation photon emissivity coefficients (PECs), often used by modellers to predict individual spectral line emission features. A PEC is a derived coefficient that is associated with a single spectral line and its excitation component (the full PEC is a combination of excitation, recombination and charge exchange components) is given by

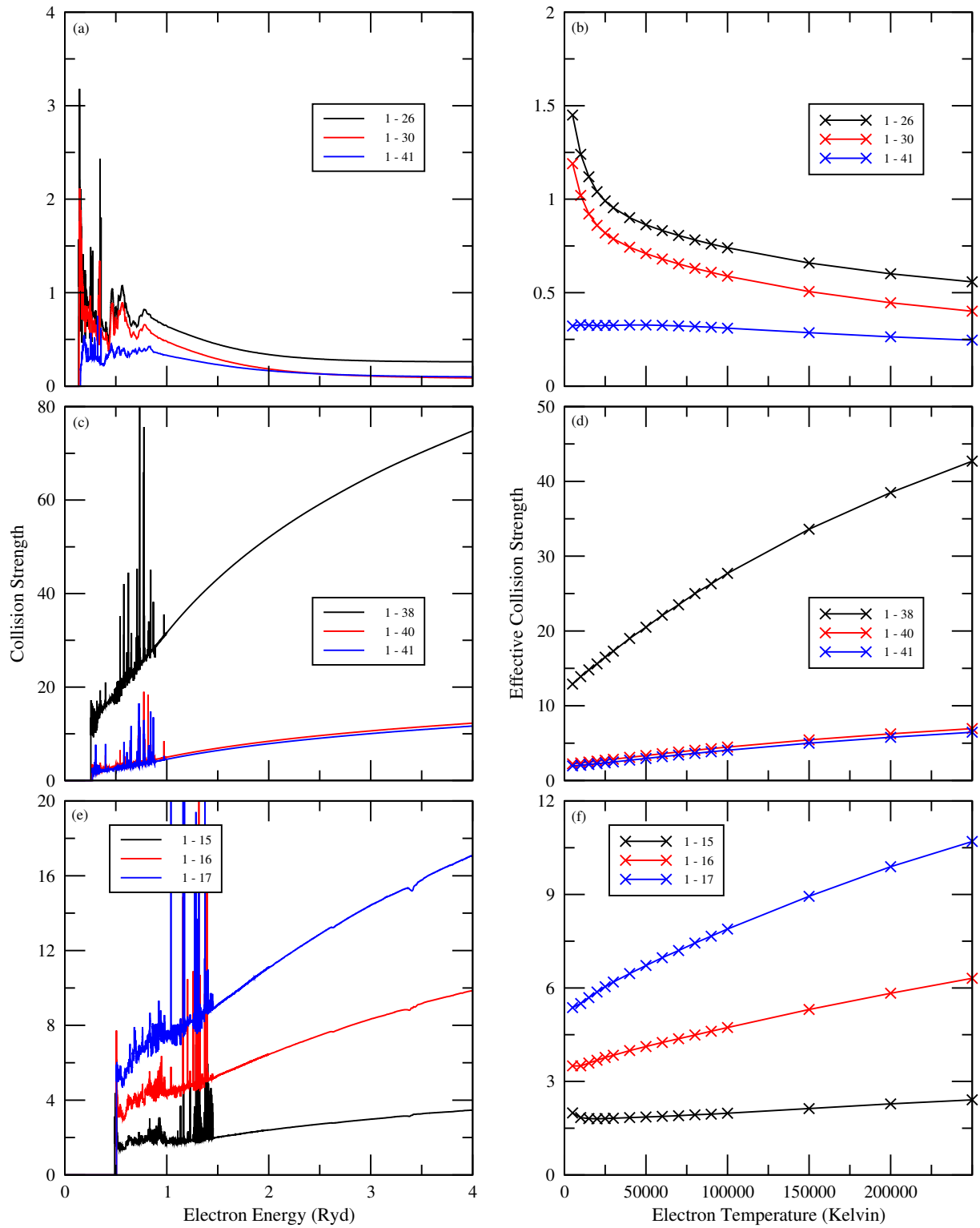


**Figure 5.** Collision strengths (left panels) and effective collision strengths (right panels) for three strong dipole transitions in Zr I-III. Results for Zr I are plotted in (a) and (b) for transitions 1-26, 1-30 and 1-41, Zr II are shown in (c) and (d) for transitions 1-38, 1-40 and 1-41, and Zr III are shown in (e) and (f) for transitions 1-15, 1-16 and 1-17. The level indices correspond to those listed in Tables 2, 3 and 4 respectively.

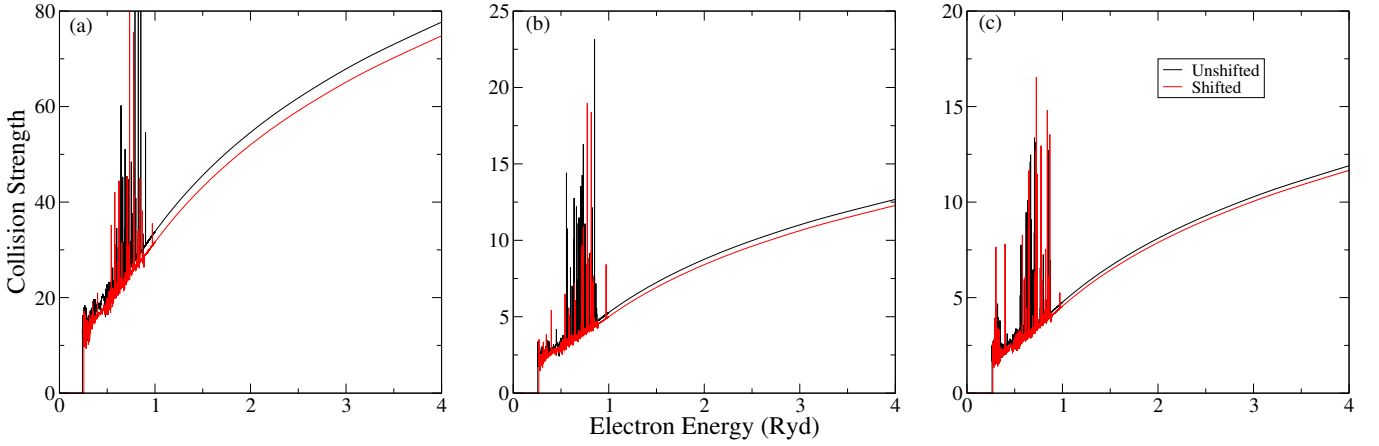


**Figure 6.** Collision strengths as a function of incident electron energy in Ryds for three transitions of Zr II. Panel (a) transition 1-38 ( $4d^25s\ 4F_{3/2}-4d^25p\ 4G_{5/2}$ ), panel (b) transition 1-40 ( $4d^25s\ 4F_{3/2}-4d^25p\ 2F_{5/2}$ ) and panel (c) transition 1-41 ( $4d^25s\ 4F_{3/2}-4d^25p\ 4F_{3/2}$ ). The black curves represent the collision strengths computed when the *ab initio* energies are adopted in the collision calculations and the red curves represent the collision strengths computed with calibrated experimental energy levels.

$$\text{PEC}_{j \rightarrow i}^{\text{excit}} = \frac{N_j^{\text{excit}} A_{j \rightarrow i}}{n_e}, \quad (2)$$

where  $N_j^{\text{excit}}$  is the weighted population of the upper level  $j$  defined so that

$$N_j^{\text{excit}} = \frac{N_j}{N_1}, \quad (3)$$

where  $N_j$  is the population of the upper level and  $N_1$  is the population of the ground state. As defined previously  $A_{j \rightarrow i}$  is the Einstein A-coefficient for the transition from  $j$  to  $i$  and  $n_e$  is the electron density in  $\text{cm}^{-3}$ . In Fig. 7 we present example synthetic spectra computed at three electron temperatures (0.25 eV, 0.5 eV and 1 eV) and an electron density of  $1 \times 10^6 \text{ cm}^{-3}$  relevant for KNe modelling. In this figure the PECs (in units  $\text{cm}^3 \text{ s}^{-1}$ ) are plotted for each of the three ion stages of Zr and the wavelength region considered ranges from 0 to 3000 nm. This range is chosen to show the bulk of the lines and important lines at longer wavelengths are discussed later, only the relative heights of lines within the same ionisation stage should be considered. Below 1000 nm a forest of Zr I, II and III lines are visible and it is in this region that most of the neutral Zr lines are found. Above 1000 nm prominent Zr II and III features are evident and appear unblended.

To further analyse these findings, we refer to a paper by Gillanders et al. (2024) in which several Zr II lines were highlighted in the 1.0 – 1.2 micron range. In that publication Table C1 listed several Zr II lines of interest, the data for which came from the Kurucz atomic database Kurucz (2024) and lines were selected based on their calculated luminosity. We have extracted this list and present them in Table 8 highlighting the relevant wavelengths, the lower and upper index labels and energies (in eV for consistency) computed in the current calculations. The associated A-values and the relative intensities of the lines that were calculated from the new data presented in this work are compared to the values in Gillanders et al. (2024), where an electron temperature of 0.43 eV ( $\sim 5000$  Kelvin) and density of  $1 \times 10^6 \text{ cm}^{-3}$  were used. Under these conditions there is agreement for the lines shown suggesting that the assumptions made in Gillanders

et al. (2024) were reasonable. The assumption of LTE can be probed by investigating the electron density dependence of the populations in these levels. This can be done using the collisional radiative theory in COLRADPY, allowing for a determination of when these levels leave LTE and enter a NLTE regime. In Fig. 8 the ratio of the population fractions and the electron density are plotted as a function of electron density ( $\text{cm}^{-3}$ ) for the levels indexed in Table 8. Clearly we can see the evolution of the population fractions as the electron density increases. When the gradient of the curve in the logarithmic plots becomes -1 the level it corresponds to is determined to be in LTE. From Fig. 8 it appears all the metastable levels considered are in NLTE for electron densities below approximately  $1 \times 10^6 \text{ cm}^{-3}$  and enter LTE for electron densities greater than this. Therefore it is likely that a fully NLTE description will be necessary at later times in the KNe evolution, as the density rapidly decreases due to the ejecta expansion.

At later stages in the evolution of the KNe the temperature decreases to such an extent that only the lowest lying target levels can be excited. To study this further we plot in Fig. 9 the PECs (in units  $\text{cm}^3 \text{ s}^{-1}$ ) computed at a low temperature of 0.1 eV (1160 Kelvin) for an extended wavelength region from 0 to 40000 nm. Clearly evident are lines between these low-lying levels which have a much greater relative intensity than the lines previously presented in Fig. 7 between 0 and 3000 nm. Prominent features of Zr I and particularly Zr II and Zr III are evident at much higher wavelengths. The relevant lines are listed in Table 9 including the wavelength, ion species, lower and upper index from the present computations and the magnitude of the PEC. All of these lines represent transitions among the lowest 4 levels of the relevant Zr charge species.

The new atomic data produced in this work can be used to predict luminosity values for prominent emission features found in the synthetic spectra. These luminosities are calculated in terms of the previously discussed PECs and are

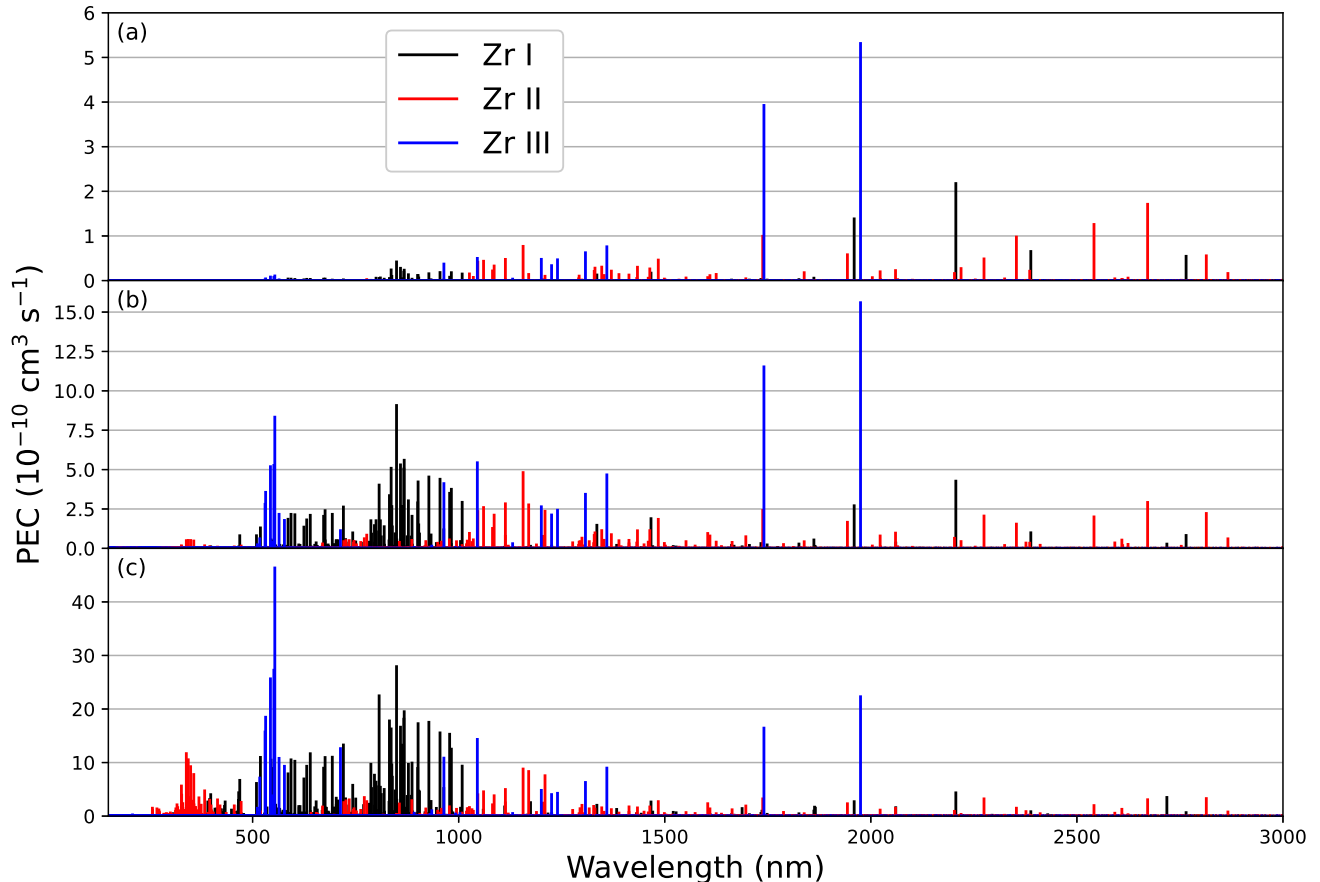


**Figure 7.** Theoretical spectra for Zr I-III with an electron density of  $1 \times 10^6 \text{ cm}^{-3}$ , where the top window (a) is for an electron energy of 0.25 eV, the middle window (b) is for 0.5 eV and the bottom window (c) is for 1 eV.

defined as,

$$L_{j \rightarrow i} = \frac{hc}{\lambda_{j \rightarrow i}} \frac{n_e \text{PEC}_{j \rightarrow i}}{\sum_i N_i} \frac{M_{\text{ion}}}{m_{\text{ion}}}, \quad (4)$$

in units of energy per time, where  $hc/\lambda$  is the photon energy,  $M_{\text{ion}}$  is the mass of the ion in the ejecta and  $m_{\text{ion}}$  is the mass of a single ion particle. The ratio of  $M_{\text{ion}}$  and  $m_{\text{ion}}$  encodes the number of ions in the ejecta. We present in Table 10 luminosity predictions for the ten most intense lines of Zr I, II and III computed at an electron temperature of 0.25 eV, an electron density of  $1 \times 10^6 \text{ cm}^{-3}$  and an ejecta mass of  $1 \times 10^{-3} M_{\odot}$ . It should be noted that the PEC values for these transitions have changed somewhat compared to Table 9, as the computations in Table 10 were performed at a higher electron temperature of 0.25 eV. We also note that the luminosity values for each species are of the same order of magnitude for all transitions,  $\approx 10^{36} \text{ erg s}^{-1}$ . These luminosity predictions for Zr can be useful when making ion-mass estimates. Additionally, referring back to Table 8 the first four highest intensity lines between 1.0 – 1.2 micron in Gillanders et al. (2024) are also included in the 10 strongest lines for Zr II predicted in Table 10.

## 5 RADIATIVE TRANSPORT

1D spectral synthesis codes such as TARDIS (Kerzendorf & Sim 2014; Kerzendorf et al. 2023) have previously been used to aid analysis of the observed spectra of AT2017gfo and to suggest identifications of spectral features, with Vieira et al. (2023) and Gillanders et al. (2024) both suggesting the presence of Zr. High quality, accurate atomic data is paramount for successful radiative transfer modelling and production of synthetic spectra. In this section, we discuss the impact our new atomic calculations have on early-time spectrum synthesis modelling by comparing with spectra previously produced using earlier datasets. We compare with the work of Gillanders et al. (2022) - hereafter referred to as G22 - following methods described by Mulholland et al. (2024). Adopting these methods, and the parameters outlined in Table 9 of that work, we produce early time spectra resembling that of AT2017gfo. We focus on early time spectra as the kilonova is still well represented by a blackbody here, an assumption important for this model. We use two atomic datasets to compare to observations, one drawn from the same sources as G22, and one where we substitute the data for Zr I - III with that presented in this work. This facilitates a direct differential test of the impact of our new atomic dataset.

Wavelength (nm)	Lower		Upper		A-value ( $s^{-1}$ )		Relative Intensity	
	Index	eV	Index	eV	This work	G24	This work	G24
1156.6	4	0.164	22	1.236	0.074	0.079	1.00	1.00
1113.7	3	0.095	21	1.208	0.065	0.066	0.60	0.62
1060.7	2	0.039	21	1.208	0.060	0.059	0.55	0.58
1046.8	1	0.000	20	1.184	0.107	0.105	0.50	0.55
1170.2	12	0.713	29	1.773	0.223	0.110	0.49	0.26
1086.3	3	0.095	22	1.236	0.033	0.035	0.45	0.47
1082.4	2	0.039	20	1.184	0.060	0.060	0.28	0.31
1026.4	1	0.000	21	1.208	0.023	0.023	0.21	0.23
1113.5	12	0.713	30	1.827	0.046	0.038	0.14	0.13
1035.8	2	0.039	22	1.236	0.009	0.010	0.13	0.14
1021.1	10	0.559	29	1.773	0.043	0.056	0.10	0.15
1120.7	10	0.559	25	1.665	0.011	0.034	0.04	0.11

**Table 8.** Zr II lines highlighted in Gillanders et al. (2024) (G24), where the index numbers represent the indexes of the levels from the Zr II calculation in this work. A comparison is made between this work and the data from Kurucz (2024) at an electron temperature of 0.43 eV ( $\sim 5000$  Kelvin) and density of  $1 \times 10^6 \text{ cm}^{-3}$ , showing reasonable agreement for these lines.

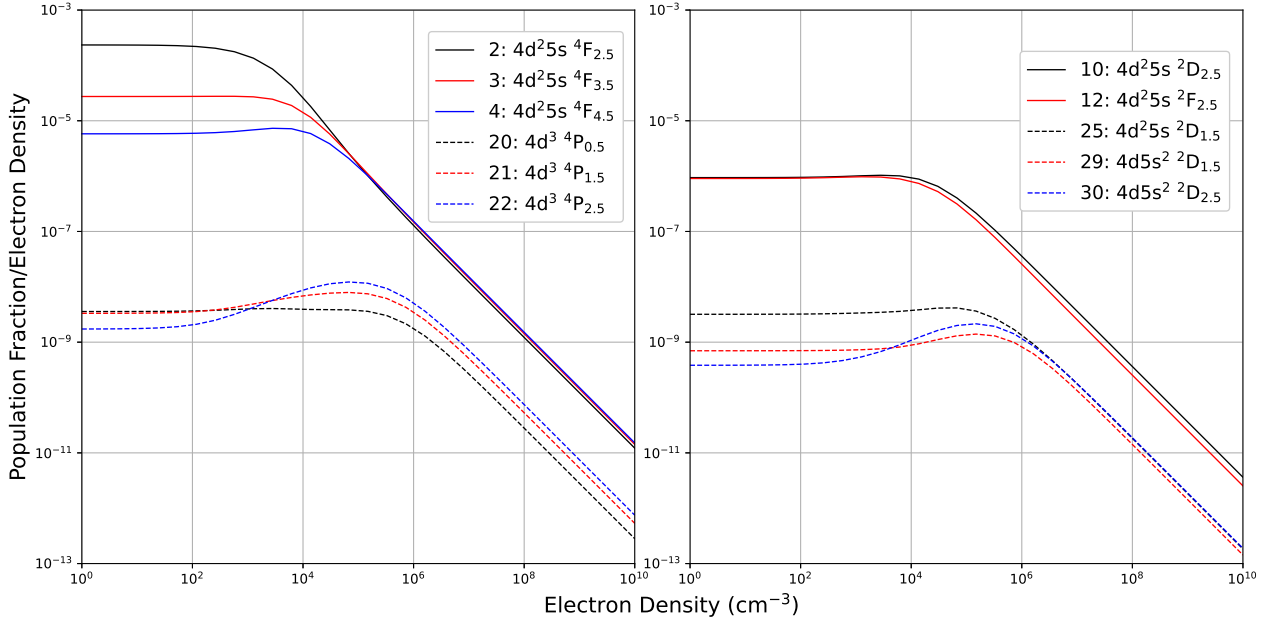


**Figure 8.** Electron density dependence of the population fractions of the metastable levels involved in transitions listed in Table 8. Calculated for an electron temperature of 0.43 eV ( $\sim 5000$  Kelvin).

Wavelength (nm)	Ion	Lower Index	Upper Index	PECs ( $\text{cm}^3 \text{s}^{-1}$ )
12424.56	Zr III	2	3	1.54E-09
14671.59	Zr III	1	2	2.56E-09
14915.82	Zr I	2	3	1.00E-09
17531.11	Zr I	1	2	1.53E-09
17874.29	Zr II	3	4	6.58E-10
22283.09	Zr II	2	3	8.80E-10
31779.15	Zr II	1	2	3.98E-10

**Table 9.** The seven lines with the largest PECs presented in Fig. 9, computed at an electron temperature of 0.1 eV and an electron density of  $1 \times 10^6 \text{ cm}^{-3}$ .

In Fig. 10 we present a line plot of the flux (in units  $10^{-16} \text{ erg s}^{-1} \text{ cm}^{-2} \text{ nm}^{-1}$ ) as a function of wavelength (in nm), at 1.4 days (left panel) and 4.4 days (right panel) post merger. Fig. 10 shows that the addition of the new data has only a small impact on the overall spectral shape, similar to previous findings for new calculations for Sr and Y (Mulholland et al. 2024). This difference is more pronounced at the earlier 1.4 day epoch, clearly seen in the inset difference plot, and is caused by changes to Zr II as the dominant ion stage at this time. By the 4.4 day epoch illustrated on the right in Fig. 10, any difference between the spectra seen in the two datasets is overshadowed by the Monte Carlo noise inherent in such simulations.

To investigate further, we construct a model with a less

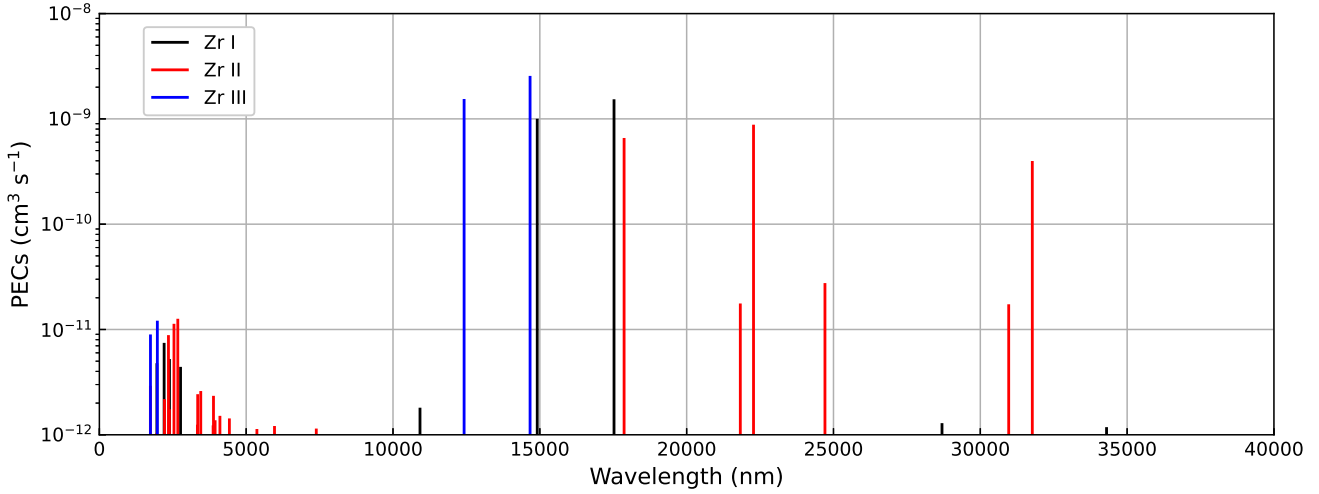


**Figure 9.** Theoretical spectra for Zr I-III with an electron temperature of 0.1 eV (1160 Kelvin) and electron density of  $1 \times 10^6 \text{ cm}^{-3}$ . This temperature is more relevant to later stages in the merger evolution, where a few lines have a relative intensity significantly greater than all the rest.

	$\lambda$ (nm)	Index ( $i-j$ )	Lower Level		Lower Level		$A_{j \rightarrow i}$ ( $\text{s}^{-1}$ )	PEC ( $\text{cm}^3 \text{s}^{-1}$ )	Luminosity ( $\text{erg s}^{-1}$ )		
			Conf.	J	E ( $\text{cm}^{-1}$ )	Conf.				J	E ( $\text{cm}^{-1}$ )
Zr I	2206.89	2 - 9	$4d^25s^2$	3.0	570.414	$4d^25s^2$	2.0	5101.676	1.56E-02	2.25E-10	2.64E+36
	14915.82	2 - 3	$4d^25s^2$	3.0	570.414	$4d^25s^2$	4.0	1240.843	6.09E-03	1.42E-09	2.47E+36
	17531.11	1 - 2	$4d^25s^2$	2.0	0.000	$4d^25s^2$	3.0	570.414	4.74E-03	1.34E-09	1.99E+36
	1960.14	1 - 9	$4d^25s^2$	2.0	0.000	$4d^25s^2$	2.0	5101.676	1.00E-02	1.44E-10	1.91E+36
	849.48	2 - 19	$4d^25s^2$	3.0	570.414	$4d^35s^1$	4.0	12342.374	9.32E-01	4.48E-11	1.37E+36
	859.05	1 - 17	$4d^25s^2$	2.0	0.000	$4d^35s^1$	2.0	11640.713	1.28E+00	3.49E-11	1.05E+36
	836.38	1 - 18	$4d^25s^2$	2.0	0.000	$4d^35s^1$	3.0	11956.329	9.16E-01	3.05E-11	9.48E+35
	868.07	3 - 21	$4d^25s^2$	4.0	1240.843	$4d^35s^1$	4.0	12760.659	1.13E+00	3.11E-11	9.30E+35
	867.16	3 - 22	$4d^25s^2$	4.0	1240.843	$4d^35s^1$	5.0	12772.774	7.29E-01	2.67E-11	7.98E+35
	2388.86	1 - 4	$4d^25s^2$	2.0	0.000	$4d^25s^2$	2.0	4186.105	2.28E-03	6.82E-11	7.41E+35
Zr II	1156.64	4 - 22	$4d^25s^1$	4.5	1322.905	$4d^3$	2.5	9968.646	7.36E-02	7.97E-11	1.79E+36
	2672.33	3 - 10	$4d^25s^1$	3.5	763.442	$4d^25s^1$	2.5	4505.495	7.88E-03	1.74E-10	1.69E+36
	1738.25	1 - 12	$4d^25s^1$	1.5	0.000	$4d^25s^1$	2.5	5752.923	8.56E-03	1.02E-10	1.53E+36
	2542.18	2 - 9	$4d^25s^1$	2.5	314.672	$4d^25s^1$	1.5	4248.304	7.70E-03	1.29E-10	1.32E+36
	17874.29	3 - 4	$4d^25s^1$	3.5	763.442	$4d^25s^1$	4.5	1322.905	4.71E-03	8.56E-10	1.24E+36
	1113.67	3 - 21	$4d^25s^1$	3.5	763.442	$4d^3$	1.5	9742.796	6.48E-02	5.06E-11	1.18E+36
	1060.66	2 - 21	$4d^25s^1$	2.5	314.672	$4d^3$	1.5	9742.796	5.95E-02	4.64E-11	1.14E+36
	2353.88	1 - 9	$4d^25s^1$	1.5	0.000	$4d^25s^1$	1.5	4248.304	6.01E-03	1.01E-10	1.11E+36
	1046.78	1 - 20	$4d^25s^1$	1.5	0.000	$4d^3$	0.5	9553.104	1.07E-01	4.43E-11	1.10E+36
	22283.09	2 - 3	$4d^25s^1$	2.5	314.672	$4d^25s^1$	3.5	763.442	3.90E-03	7.61E-10	8.86E+35
Zr III	1975.58	2 - 4	$4d^2$	3.0	681.589	$4d^2$	2.0	5743.387	3.08E-02	5.33E-10	7.01E+36
	12424.56	2 - 3	$4d^2$	3.0	681.589	$4d^2$	4.0	1486.447	1.05E-02	2.96E-09	6.18E+36
	1741.13	1 - 4	$4d^2$	2.0	0.000	$4d^2$	2.0	5743.387	2.28E-02	3.95E-10	5.89E+36
	14671.59	1 - 2	$4d^2$	2.0	0.000	$4d^2$	3.0	681.589	8.08E-03	2.76E-09	4.88E+36
	1359.89	3 - 7	$4d^2$	4.0	1486.447	$4d^2$	2.0	8839.967	2.24E-02	7.87E-11	1.50E+36
	1045.57	3 - 8	$4d^2$	4.0	1486.447	$4d^2$	4.0	11050.568	2.46E-02	5.28E-11	1.31E+36
	1307.95	2 - 6	$4d^2$	3.0	681.589	$4d^2$	1.0	8327.117	2.35E-02	6.54E-11	1.30E+36
	1200.90	1 - 6	$4d^2$	2.0	0.000	$4d^2$	1.0	8327.117	1.82E-02	5.07E-11	1.09E+36
	964.42	2 - 8	$4d^2$	3.0	681.589	$4d^2$	4.0	11050.568	1.87E-02	4.01E-11	1.08E+36
	1240.14	1 - 5	$4d^2$	2.0	0.000	$4d^2$	0.0	8063.628	4.65E-02	4.96E-11	1.04E+36

**Table 10.** Luminosities for the ten strongest lines from each Zr ion considered here at  $T_e = 0.25 \text{ eV}$ ,  $n_e = 1 \times 10^6 \text{ cm}^{-3}$  and a mass of  $1 \times 10^{-3} M_\odot$ .

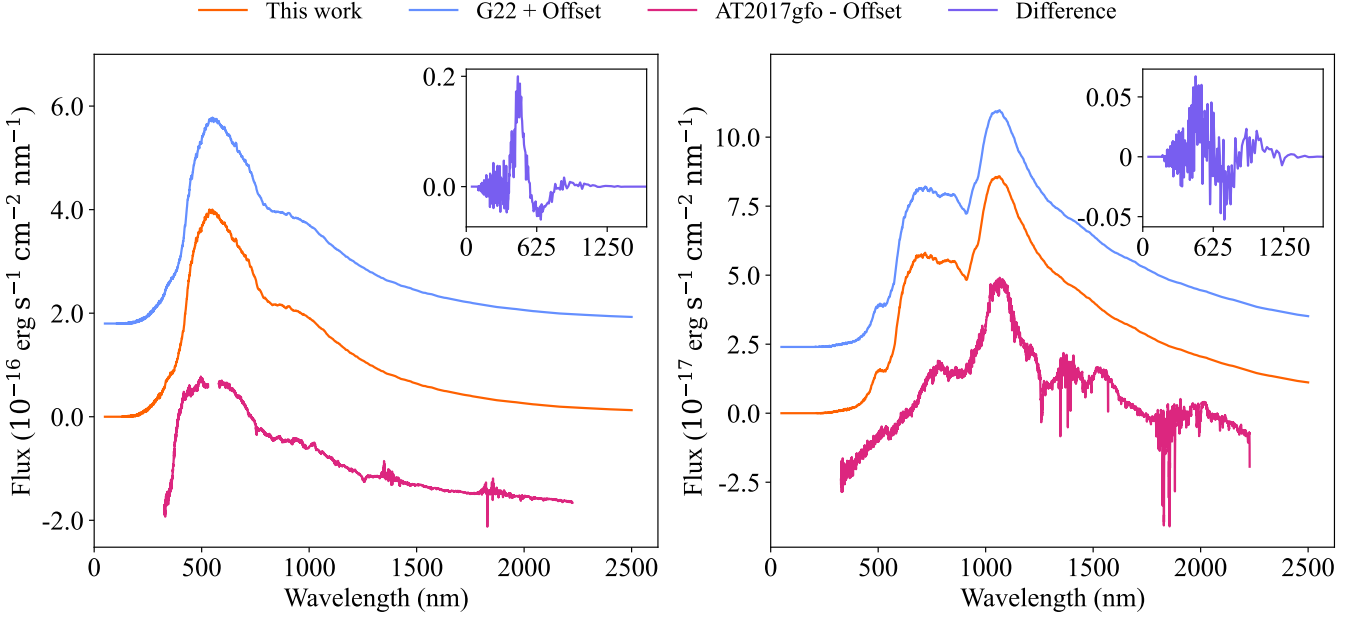


**Figure 10.** Line plot showing a comparison between a realistic elemental composition of AT2017gfo at 1.4 days (left) and 4.4 days (right) post-merger. The spectrum produced from the same atomic data sources as used by G22 is shown in blue, with the data set including the new calculation presented in this work for Zr shown in orange, alongside the observed spectrum (Pian et al. 2017; Smartt et al. 2017) in pink. These observations and synthetic spectra from the G22 dataset have been arbitrarily offset from the spectrum featuring the new calculation - by  $\mp 1.8$  E-16 erg  $s^{-1}$   $cm^{-2}$   $nm^{-1}$  at 1.4 days and  $\mp 2.4$  E-17 erg  $s^{-1}$   $cm^{-2}$   $nm^{-1}$  at 4.4 days - for visual clarity. We note there is a visual discrepancy between the simulated spectra and the observations: this is due to using a more recent version of TARDIS, with an improved relativistic treatment (Vogl et al. 2019). Both datasets are treated with this same updated relativity to allow for comparison. An inset plot is included showing the difference between the two synthetic spectra in purple.

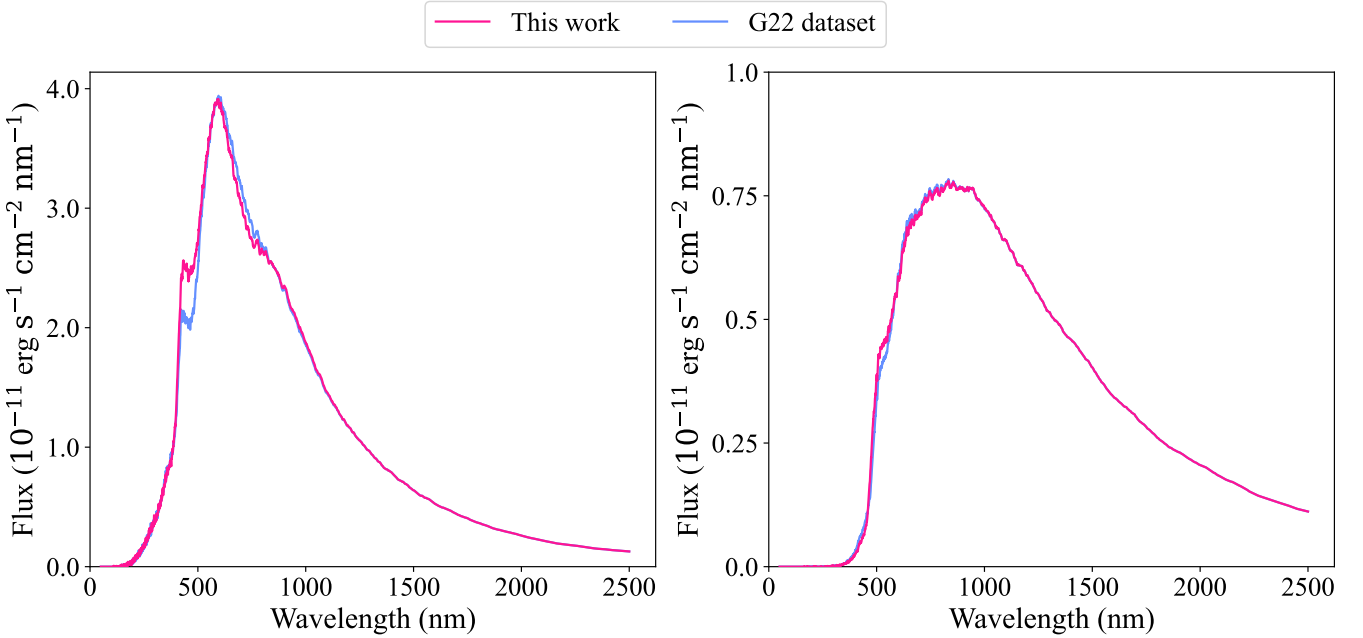


**Figure 11.** Comparison between pure Zr models of AT2017gfo at 1.4 days (left) and 4.4 days (right) showing differences between data used by G22 (blue) and this calculation (pink). The spectra shown here are dominated by Zr II.

realistic composition, a pure Zr KNe, to isolate the effect the new data from these new calculations have on the spectra. In Fig. 11, we again see the strongest difference between the dataset used by G22 and this new simulation in the region around 500 nm at the 1.4 day observational epoch, with this difference becoming much less pronounced by the 4.4 day time frame. In summary, whilst we find only small changes in the synthetic spectra by substituting the new atomic datasets into the radiative transfer models of AT2017gfo, future further refinements to the atomic data available for such models may have a cumulative, visible effect on synthetic spectra and models, particularly with future efforts to push more towards modelling in full NLTE.

## 6 CONCLUSIONS

Recent interest in NLTE modelling of the KNe from NSM events have motivated this study on the structure and electron-impact excitation of the first three ion stages of Zr. Atomic structure calculations using GRASP0 produced the required energy levels and transition rates, and further collision calculations using DARC provided the excitation and de-excitation rates for Zr I, Zr II and Zr III. All these atomic data are vital for the accurate modelling of these events.

The functionality in both the GRASP0 and DARC codes to calibrate the target state energies to their exact experimental positions was adopted, thereby producing spectroscopically accurate wavelengths and therefore more accurate A-values and collision strengths. A detailed analysis of the difference between adopting shifted or unshifted energies was carried out with regard to the computation of A-values for transitions among the target levels and the corresponding electron-impact excitation collision strengths. For all species it was revealed that the most significant impact was in the resulting A-values, whereas the changes in the collision strengths was relatively small. We conclude that, if possible, target energies should be calibrated to their spectroscopic positions to maximize the accuracy of the results and aid in the identification of observed spectral features.

The atomic data produced for Zr I-III was further incorporated into a collisional radiative model using the COLRADPY code to compute populations for the ground and metastable levels, derive PECs across a wide wavelength region and finally use these PECs to compute luminosity values for prominent line candidates in the synthetic spectra. All of this modelling was performed for electron temperatures and densities of relevance to KNe events. The transitions listed in Table 8 were found to be in LTE for electron densities greater than  $1 \times 10^6 \text{ cm}^{-3}$  but for densities lower than this value NLTE modelling would be required.

Finally the new atomic datasets were incorporated into a 1D radiative transfer simulation using the TARDIS suite of computer packages. The addition of the new data had only a small impact on the overall spectral shape during photospheric phases, with the greatest differences occurring at the early observational epoch of 1.4 days post merger. By 4.4 days any differences could be attributed to Monte Carlo noise. These small differences for three lone Zr species could, however, produce a cumulative effect as more and more accurate atomic data calculations are produced in the future. This is

particularly important as current efforts move more towards modelling in full NLTE.

## ACKNOWLEDGEMENTS

Funded/Co-funded by the European Union (ERC, HEAVYMETAL, 101071865). Views and opinions expressed are however those of the author(s) only and do not necessarily reflect those of the European Union or the European Research Council. Neither the European Union nor the granting authority can be held responsible for them. This research made use of TARDIS, a community-developed software package for spectral synthesis in supernovae (Kerzendorf & Sim 2014; Vogl et al. 2019; Kerzendorf et al. 2023). The development of TARDIS received support from the Google Summer of Code initiative and from ESA's Summer of Code in Space program. TARDIS makes extensive use of Astropy and PyNE.

## DATA AVAILABILITY

The data presented in this work will be made available in the OPEN-ADAS (2024) database or included with the current iteration of the R-matrix codes on the DARC website (Ballance 2024), in the form of adf04 files compatible with the ADAS suite of codes or the open-source ColRadPy (Johnson et al. 2019).

## REFERENCES

- Ballance C. P., 2024, R-matrix codes, <http://connorb.freeshell.org>
- Biémont E., Grevesse N., Hannaford P., Lowe R. M., 1981, *Astrophysical Journal*, 248, 867
- Burgess A., 1974, *Journal of Physics B: Atomic and Molecular Physics*, 7, L364
- Burke P. G., 2011, R-Matrix Theory of Atomic Collisions: Application to Atomic, Molecular and Optical Processes. Springer Series on Atomic, Optical, and Plasma Physics Vol. 61, Springer-Verlag Berlin Heidelberg, <https://www.springer.com/gp/book/9783642159305>
- Gillanders J. H., Smartt S. J., Sim S. A., Bauswein A., Goriely S., 2022, *MNRAS*, 515, 631
- Gillanders J. H., Sim S. A., Smartt S. J., Goriely S., Bauswein A., 2024, *Monthly Notices of the Royal Astronomical Society*, 529, 2918
- Johnson C., Loch S., Ennis D., 2019, *Nuclear Materials and Energy*, 20, 100579
- Kajino T., Aoki W., Balantekin A., Diehl R., Famiano M., Mathews G., 2019, *Progress in Particle and Nuclear Physics*, 107, 109
- Kerzendorf W. E., Sim S. A., 2014, *Monthly Notices of the Royal Astronomical Society*, 440, 387
- Kerzendorf W., et al., 2023, tardis-sn/tardis: TARDIS v2023.08.13, doi:10.5281/zenodo.8244935, <https://doi.org/10.5281/zenodo.8244935>
- Kramida A., Ralchenko Y., Reader J., NIST ASD Team 2024, NIST Atomic Spectra Database (version 5.11), <https://physics.nist.gov/asd>
- Kurucz R. L., 2024, Kurucz Atomic Database (version 5.11), <http://kurucz.harvard.edu/atoms.html>
- Lawler J. E., Schmidt J. R., Hartog E. A. D., 2022, *Journal of Quantitative Spectroscopy and Radiative Transfer*, 289, 108283



- Ljung G., Nilsson H., Asplund M., Johansson S., 2006, *A&A*, 456, 1181
- Moore C. E., 1971, in , Nat. Stand. Ref. Data Ser., NSRDS-NBS 35, Vol. II (Reprint of NBS Circ. 467, Vol. II, 1952). Nat. Bur. Stand., U.S., doi:10.6028/NBS.NSRDS.35v2
- Mulholland L. P., McElroy N. E., McNeill F. L., Sim S. A., Ballance C. P., Ramsbottom C. A., 2024, *Monthly Notices of the Royal Astronomical Society*, 532, 2289
- Norrington P. H., Grant I. P., 1987, *Journal of Physics B: Atomic and Molecular Physics*, 20, 4869
- OPEN-ADAS 2024, OPEN-ADAS website, <https://open.adas.ac.uk>
- Parpia F. A., Froese Fischer C., Grant I. P., 1996, *Comp. Phys. Comm.*, 94, 249
- Pian E., et al., 2017, *Nature*, 551, 67
- Pognan Q., Grumer J., Jerkstrand A., Wanajo S., 2023, *Monthly Notices of the Royal Astronomical Society*, 526, 5220
- Reader J., Acquista N., 1997, *Physica Scripta*, 55, 310
- Smartt S. J., et al., 2017, *Nature*, 551, 75
- Summers H. P., et al., 2006, *Plasma Physics and Controlled Fusion*, 48, 263
- Vieira N., Ruan J. J., Haggard D., Ford N., Drout M. R., Fernández R., Badnell N. R., 2023, *The Astrophysical Journal*, 944, 123
- Vogl C., Sim S. A., Noebauer U. M., Kerzendorf W. E., Hillebrandt W., 2019, *A&A*, 621, A29

This paper has been typeset from a  $\text{\TeX}/\text{\LaTeX}$  file prepared by the author.